Alteration of Bakken reservoir rock during CO_2-based fracturing—An autoclave reaction experiment

CrossMark

Jiemin Lu [a,*], Jean-Philippe Nicot [a], Patrick J. Mickler [a], Lionel H. Ribeiro [b], Roxana Darvari [a]

[a] Bureau of Economic Geology, Jackson School of Geosciences, The University of Texas at Austin, Austin, TX, United States
[b] Statoil, Research and Technology, Houston, TX, United States

ARTICLE INFO

ABSTRACT

This study was conducted to document and assess the effects of fluid–rock interactions when CO_2 is used to create the fractures necessary to produce hydrocarbons from low-permeability rocks. The primary objectives are to (1) identify and understand the geochemical reactions of CO_2-based fracturing, and (2) assess potential changes in porosity and permeability of formation rock. Autoclave experiments were conducted at reservoir conditions exposing middle Bakken core fragments to CO_2-saturated synthetic formation brine and to supercritical CO_2 (sc-CO_2) only. Ion-milled core samples were examined before and after the reaction experiments using scanning electron microscopy (SEM), which enabled us to image the reaction surface in extreme detail and unambiguously identify mineral dissolution and precipitation.

The most significant change in the reacted samples exposed to the CO_2-saturated brine is dissolution of the carbonate minerals, particularly calcite, which shows severe corrosion. Dolomite grains were corroded to a lesser degree. Quartz and feldspars remained intact, and some pyrite framboids underwent slight dissolution. Additionally, a small amount of calcite precipitation took place, as indicated by numerous small calcite crystals formed at the reaction surface and in the pores. The changes of aqueous chemical composition are consistent with the petrographic observations with an increase in Ca and Mg and associated minor elements, and a very slight increase in Fe and sulfate.

When exposed to sc-CO_2 only, changes observed include etching of the calcite grain surface and precipitation of salt crystals (halite and anhydrite) due to evaporation of residual pore water into the sc-CO_2 phase. Dolomite and feldspars remained intact, and pyrite grains were slightly altered. Mercury intrusion capillary pressure (MICP) tests on reacted and unreacted samples show an increase in porosity when an aqueous phase is present but no overall porosity change with sc-CO_2. The results also show an increase in permeability for brine-reacted samples.

1. Introduction

Although water is by far the most dominant fluid used to stimulate low-permeability rocks, several other types of fluids have been tested, for example, liquefied petroleum gas/propane, CO_2, and N_2. CO_2 fracturing has been tested in the field since the early 1960's (Harris et al., 1984; Garbis and Taylor, 1986; Sinal and Lancaster, 1987; Liao et al., 2009; Ribeiro et al., 2015). The use of CO_2 for hydraulic fracturing (HF) applications is now gaining popularity in several unconventional reservoirs such as the middle Bakken (Jacobs, 2014). Although the amount of water used per unit of energy produced is relatively small for HF in the Bakken play

(Scanlon et al., 2014), the western half of North Dakota, where the play is located, has a semi-arid climate and the potential of using supercritical CO_2 (sc-CO_2) as an alternative to water in HF could alleviate water concerns. Besides reduction of water usage, another major benefit of using CO_2 as a fracturing fluid is to prevent potential reduction of formation permeability due to water imbibition and to increase production (Sinal and Lancaster, 1987; Liao et al., 2009; Cheng, 2012; Ribeiro and Sharma, 2012).

CO_2 has been successfully used for decades, in particular in the Permian Basin, for miscible flooding to increase oil recovery. In addition, CO_2 has been proposed as a circulation fluid for geothermal energy extraction (Brown, 2000, 2003; Pruess, 2006; Atrens et al., 2008). Some recent research has also investigated using shales and other tight formations as storage formations in the context of CO_2 capture and storage (Sun et al., 2013; Middleton et al., 2014). The rock-forming materials in unconventional

reservoir rocks are not unique and can be found in conventional reservoir rocks, though relative abundance of mineral phases and organic matter varies. In terms of geochemical reactions with CO_2 and brine, there is no fundamental difference between unconventional (shales, tight sands) and conventional (sandstones, carbonates) reservoir rocks. The same reaction pathways of sandstones also applies to shales. Generally, when CO_2 enters rock formations, it will dissolve into the formation water and quickly lower the pH (Kharaka and Cole, 2011). Dissolution of CO_2 initiates a variety of geochemical reactions between pore waters and formation minerals. Geochemical interactions caused by injection of CO_2 into water-saturated formations have been studied by numerical modeling (Gunter et al., 1997; Xu et al., 2003, 2005, 2010; Johnson et al., 2005; Knauss et al., 2005; White et al., 2005; Zhang et al., 2015), laboratory experiments (Fischer et al., 2010; Lu et al., 2010, 2014; Chopping and Kaszuba, 2012; Yu et al., 2012; Jun et al., 2013; Huq et al., 2015), and field tests (Emberley et al., 2005; Kharaka et al., 2006; Mito et al., 2008; Lu et al., 2012) in the context of geological CO_2 sequestration. However, the impact of sc-CO_2 on the flow property of reservoir rocks is not as well documented in the literature (Wang et al., 2013). The overall reactivity of tight rocks and CO_2-saturated brine can also be different from that of porous rocks because of the small grain size and low permeability.

The main objective of this study was to determine the impact of "dry" CO_2 and CO_2-saturated brine on the Bakken reservoir rock, and potentially on oil production, in comparison with water-based reactions. Three autoclave experiments were conducted to assess fluid–rock interactions when CO_2 instead of water is used for fracturing in the Bakken formation. It is generally believed that sc-CO_2 by itself will not interact much with the rock beyond sorption. However, the presence of water, e.g., formation water, which facilitates many geochemical reactions, can impact production favorably (if dissolution dominates) or negatively (if reprecipitation dominates). Bakken core samples were exposed to CO_2-saturated brine and to dry CO_2. The experimental results provide insights on the physical and chemical interactions between rock matrix and CO_2.

2. Material and sample

The Bakken formation is composed of three members: a lower shale; a middle member comprising sandstones, siltstones, dolomite, and shale; and an upper shale. Many wells are also completed in the underlying Three Forks formation. This study uses core samples from a well completed in 2015 in the middle Bakken member, which is the most common reservoir target stimulated through HF in the Bakken play. The core was provided by Statoil from a well drilled in Williams County in North Dakota (Fig. 1) to a depth >10,000 ft. The core sample provided by the sponsor is a very fine grained sandstone with abundant carbonate cement. The reservoir pore pressure is >550 bars, and the temperature is 115 °C. The experiments were conducted at the same temperature but at lower pressure (300 bars) because of experimental limitations.

3. Methods

Rock samples in the autoclave experiments were analyzed—first on a fresh unreacted sample, then on reacted samples—using a variety of tools: X-ray diffraction (XRD), mercury intrusion capillary pressure (MICP), and scanning electron microscopy (SEM) coupled with X-ray energy-dispersive spectroscopy (EDS) complemented by argon ion milling for sample preparation. Quantitative XRD analysis of spray-dried random powders provides good estimates of the amount of the most abundant minerals

(for example, quartz, feldspars, carbonates, clays) but not necessarily of minerals in minute amounts (less than ~1–2%) such as pyrite or, perhaps, anhydrite. SEM on ion-milled samples produces sharp images showing the topography of a microscopic surface, allowing the visual determination of mineralogy and texture. EDS gives the elemental composition of the surface of a sample and allows the creation of maps of elements of interest, for example, Fe or Ca distribution. No particular precaution was taken when handling the cores and rock fragments. Sample preparation methods and analytical parameters can be found in Lu et al. (2011, 2012, 2014).

3.1. X-ray diffraction

Bulk powders of the original and reacted rock samples were prepared for quantitative XRD analysis by wet grinding and spray drying, following the procedures outlined in Hillier (1999). Core fragments were first disintegrated using a TEMA ball mill before further grinding in a McCrone Micronizing Mill. Samples were ground for 16 min in a 0.5% (wt./vol) aqueous solution of polyvinyl alcohol to sufficiently reduce particle size to less than 10 μm. The resulting slurry samples were sprayed into the top of a spray drier, and the resulting dry and randomly oriented powders were collected at the bottom. XRD analysis was conducted on a Bruker AXS D8 diffractometer at The University of Texas at Austin. Bruker's Eva software was used to identify mineral phases. Quantitative analysis was conducted using Topas 3, a personal computer software based on the Rietveld method (Bish, 1994).

3.2. Mercury intrusion capillary pressure

Pore systems and capillary properties of the samples were characterized with high-pressure MICP measurements at PoroTechnology, using techniques similar to Shafer and Neasham (2000). MICP permeability was calculated using the modified Purcell method (Comisky et al., 2007). All samples were dried at ~100 °C prior to MICP tests. MICP was increased in a stepwise manner, and the percentage of rock volume saturated by mercury at each step was recorded, after allowing sufficient time for equilibrium to be established.

3.3. Scanning electron microscopy of ion-milled samples

For each experiment, a piece of unreacted shale shaped in a cuboid of approximately $10 \times 8 \times 5$ mm in size was ion milled and examined by SEM. Unreacted samples were first polished by a triple ion beam miller (Leica EM TIC020) using an accelerating voltage of 8 kV, a current of 2.8 mA, and a milling time of 10 h. The polished surfaces were perpendicular to the beddings and showed as shallow triangles of ~5 mm long and ~1 wide. Iridium was sputtered on the ion-milled surfaces to create a conductive coating to limit charging during SEM imaging. Unreacted samples were examined by SEM with the aid of an X-ray EDS system. Secondary electron (SE) images, backscattered electron (BSE) images, and EDS elemental maps were obtained with location reference. Then, the coated surfaces were remilled using a broad ion beam miller (Leica EM TIC 3X) to remove the iridium coating. Remilled surfaces were examined with a low-vacuum SEM detector in a water–vapor environment. After two rounds of SEM imaging, each of the eight polished, uncoated shale cuboids was placed in the reaction vessel with other core fragments (16 g in total) to react with the brine for over 3 weeks.

After a reacted sample was retrieved from the reactor, the ion-milled surface was examined using the low-vacuum SEM detector without a conductive coating. SEM images were taken at the exact same areas at which the prereaction images had been taken. By directly comparing the topography of the same areas of unreacted
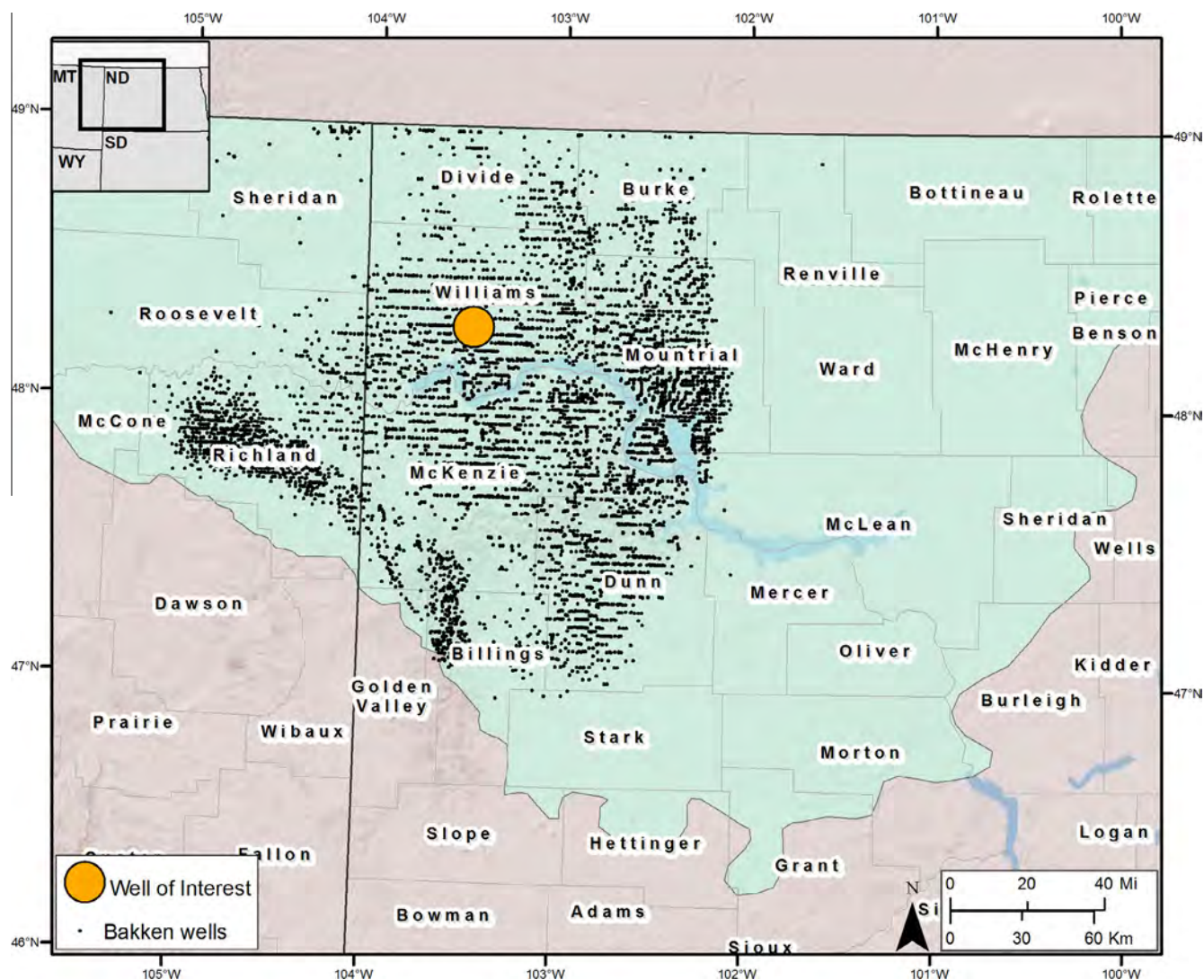
Fig. 1. Location map of cored well.

and reacted rock samples without a veil of coating material, we were able to identify mineral dissolution and precipitation that occurred during the reaction experiments.

Samples with iridium coating were examined on an FEI Nova-Nano SEM 430 using SE and BSE modes at an accelerating voltage of 10–15 kV and a working distance of 7–9.5 mm. X-ray EDS mapping was conducted using dual Bruker 30-mm^2 detectors. Mineral composition was documented by BSE and EDS images in prereaction samples. Uncoated samples were examined under low-vacuum conditions (chamber pressure = 0.35 Torr) with water vapor as conductive media. Low accelerating voltage (4 kV) of the electron source beam was used, and working distance was set at 3.2 mm. Mineralogical identification is greatly hindered in this mode because low accelerating voltage leads to a weak BSE signal and incomplete EDS spectra. However, without a layer of coating material overlying the polished surface, low-vacuum detector (LVD) images reveal more topographic and textural details, and the boundaries of fine grains and contacts between different components are more readily observed. A different charging effect helps identify calcite, which usually shows a bright charging effect in larger grains; because smaller calcite grains do not glow as much, lower water–vapor pressure is required for the charge effect to show up.

For the reacted sample with only sc-CO$_2$ (Exp-C), an extra procedure of iridium coating was applied to enable EDS analysis after

the reaction experiment. EDS analysis on the reacted sample helped to identify the salt precipitated at the reaction surface.

3.4. Fluid chemical analyses

Major cations and anions of water samples were analyzed on two Dionex ICS-1100 Ion Chromatography (IC) systems equipped with an Dionex AS-AP auto sampler. Aqueous samples were diluted ∼900 times after collection. Trace elements were analyzed on an Agilent 7500ce quadrupole inductively coupled plasma mass spectrometer (ICP-MS). Samples for trace metals were diluted ∼1000 times with 2% HNO$_3$ immediately after collection so that the total dissolved solid content was close to 500 ppm.

The pH was determined using an Orion 3-star pH meter and gel-filled pH/ATC Triode on ∼2 mL purged water at room temperature and atmospheric pressure. Dissolved inorganic carbon (DIC) was analyzed on ∼1.5 mL aliquot by a carbon analyzer.

4. Experiment setup

Rock fragments were extracted from the center of the core section to limit contamination by drilling muds. Four experiments were conducted (Table 1): two with synthetic brine and CO$_2$

(Exp-A and Exp-B) and two with CO_2 only (Exp-C and Exp-D). Exp-D, a repeat of Exp-C, was conducted using core fragments to provide samples for MICP and XRD analyses that were not done with Exp-C.

Given the difficulties of collecting a sufficient amount of formation brine not impacted by HF fluids, a synthetic brine was used for Exp-A and B; it was made with NaCl, $CaCl_2$, and KCl salts dissolved into deionized water to approximately match the concentration of Na, Ca, K, and Cl in the formation water described in the dataset provided by the sponsor (Table 2). The salinity of the synthetic brine was ~200,000 ppm. Reflecting the impurities in the salts used to make the synthetic brine, other cations and anions (Li, B, Mg, Al, Si, P, Fe, Cu, sulfate) were present at the ppm level, with relatively high levels of Br (~250 ppm) and Sr (~150 ppm). The brines for Exp-A and B were made separately; therefore, there are small differences in the chemical composition between them due to the slight variations in the weight of the salts used for making the solutions.

For each autoclave experiment (except Exp-D), an argon ion-milled shale block was prepared and examined using SEM before and after the reaction experiment. The flat surface of the ion-milled area allowed us to locate and compare the same area imaged before the experiments. The ion-milled rock blocks were reacted with other unprepared rock chips (in total, ~8 g for each experiment), which were retrieved for XRD and MICP tests after the experiments.

The experiments were conducted at 115 °C and 300 bars with either synthetic brine and CO_2 or CO_2 only. The schematic diagram of the experiment apparatus is shown in Fig. 2. Approximately 8 g of rock fragments, usually consisting of two to four core fragments with a small ion-milled block, were loaded into a quartz liner in the reaction vessel with brine or no water. The rock chips were not disintegrated in order to keep the mineral surface area relatively unchanged and to minimize the risk of plugging the lines of the sampling system. For the brine and CO_2 experiments (Exp-A and Exp-B), 110 mL synthetic brine was then added, giving a bulk brine/rock volume ratio of ~34, higher than in an actual HF operation. Nitrogen (N_2) was flushed through the reaction vessel for 5–10 min to remove residual atmospheric gasses such as O_2. The vessel was then sealed and pressurized to 300 bar using a high-pressure N_2 tank, and the temperature was increased to 115 °C. Exp-A reacted the core chips with synthetic brine under N_2 headspace for 3 days before adding CO_2, while in Exp-B, the rock sample reacted with the brine for 8 days before CO_2 was added. Exp-C and Exp-D did not use brine, and the rock samples were submerged in dry sc-CO_2 for the whole duration of each experiment.

Temperature and pressure were controlled by regulators. The reaction temperature was maintained by a computer-controlled heater with a thermocouple positioned in the reaction chamber. A magnetic stirrer wrapped in a PEEK sleeve with two blades homogenized the system and speeded reactions by removing slow diffusion-based controls.

One aqueous sample was taken through a dip tube in the reactor, as baseline immediately after the rock and brine were loaded to the reaction vessel. Another was taken right before CO_2 injection. The other aqueous samples were taken with decreasing frequency during the experiments. Approximately 2 mL of fluid was purged through the sampling port to remove the old fluid isolated in the sampling tubing. The purged fluid was set aside and used for pH measurement. After the purge, approximately 2 mL of fluid was collected for analyses of IC, ICP, and DIC. No additional fluid was added during the experiments.

5. Results

Because CO_2 is a reactive gas, we anticipated that its dissolution in water would decrease the solution pH, attack carbonates and other minerals, and mobilize other chemical elements that may or may not stay in solution at the projected low pH (<4). On the other hand, as reactions generally need an aqueous medium in which to proceed, we expected that sc-CO_2 by itself would not interact much with the rock beyond sorption. However, the presence of a small amount of water, e.g., residual pore water, may cause changes.

5.1. Description of unreacted samples

The studied core is a very fine grained sandstone heavily cemented by dolomite and calcite (Fig. 3). Detrital grains mainly consist of subrounded quartz and small amounts of K-feldspar and plagioclase (Fig. 3a and b). Dolomite, marked as olive in the EDS element maps, often occurs as euhedral and semi-euhedral crystals showing growth bands. Calcite, tagged in red, occurs mostly as pervasive cement. Pyrite (yellow) occurs mostly as euhedral crystals and as a small number of framboids. The majority of matrix materials consist of illite, mica, and clay-sized K-feldspar, quartz, and carbonate minerals.

Porosity is low because most of the primary pores are filled with carbonate cements, pyrite, and clay-sized materials (Fig. 3c and d). Observed pores consist chiefly of primary intergranular pores partially filled with cements and fines (Fig. 3e). Submicron intraparticle pores are present in authigenic dolomite and calcite grains (Fig. 3f).

5.2. Reaction with brine and CO_2 (Exp-A and Exp-B)

By locating characteristic mineral grains in the reacted samples, SEM images were taken at the exact areas previously imaged before the reaction experiments (Figs. 4 and 5). Mineral dissolution and precipitation were determined by comparing the two sets of images.

The two brine–CO_2 experiments showed similar impacts by the reaction fluids. Both sample surfaces were heavily corroded. The most significant impact of the reaction surface was corrosion of carbonate cements. The newly formed dissolution pits and holes were mostly located at the sites of preexisting calcite and dolomite cements. All calcite grain surfaces were severely corroded, and some small grains were completely dissolved. Corroded grain surfaces were marked with dense dissolution grooves and steps. Most dolomite grains were corroded at the surface, but the major part of the grains survived the reaction (Fig. 4c and i). Corroded dolomite surfaces were covered with submicron crystals lined up along lattice. For example, in Fig. 4i, the profile of rhombic dolomite in the center was lowered by dissolution. The corroded grain surface was densely dotted by small dolomite crystals.

Little dissolution occurred to feldspar minerals whose ion-milled surfaces remained intact, without any dissolution pits or grooves. Although pyrite crystals and framboids were largely

Table 1
Conditions of autoclave experiments.

Experiment	Rock (g)	Brine (mL)	Brine stage (days)	CO_2 stage (days)	Pressure (bar)	Temperature (°C)
A	8.04	110	3	21	300	115
B	8.01	110	8	22		
C	8.05	CO_2 only	N/A	23		
D	10.20	CO_2 only	N/A	22		

Table 2
Chemical composition of synthetic brine used in Exp-A and Exp-B runs.

Synthetic brine IC results (BDL = below detection limit)

Sample	Li (ppm)	Na (ppm)	NH4 (ppm)	K (ppm)	Mg (ppm)	Ca (ppm)	F (ppm)	Cl (ppm)	NO2 (ppm)	Br (ppm)	NO3 (ppm)	PO4 (ppm)	SO4 (ppm)
Exp-A	5.0	57,508	BDL	4641	2.1	9150	BDL	115,306	BDL	247.3		BDL	Tr.
Exp-B	5.6	52,700	BDL	4299	5.5	9243	BDL	106,039	BDL	262.		BDL	Tr.

Synthetic Brine ICP Results (⩽detection limit, N.A. = not analyzed, orange highlighted = above calibration)

Sample	Li (ppm)	B (ppm)	Na (ppm)	Mg (ppm)	Al (ppm)	Si (ppm)	P (ppm)	K (ppm)	Ca (ppm)	Ti (ppm)	V (ppm)
Exp-A	7.4	8.9	59,587	3.8	2.7	19.9	2.1	4735	8711	0.10	<0.006
Exp-B	7.6	10.1	54,390	3	2	20.4	3.4	4633	9358	0.10	

Sample	Cr (ppm)	Mn (ppm)	Fe (ppm)	Co (ppm)	Ni (ppm)	Cu (ppm)	Zn (ppm)	As (ppm)	Se (ppm)	Rb (ppm)	Sr (ppm)	Zr (ppm)
Exp-A	0.06	0.06	2.8	<0.02	0.3	1.9	0.15	<0.04	<0.007	0.75	155	<0.02
Exp-B	0.07	0.05	1.5	0.01	0.2	0.6	0.25			0.8	159	0.0008

Sample	Mo (ppm)	Ag (ppm)	Cd (ppm)	Sn (ppm)	Sb (ppm)	Cs (ppm)	Ba (ppm)	Tl (ppm)	Pb (ppm)	Bi (ppm)	Th (ppm)	U (ppm)
Exp-A	0.17	<1.52	<0.02	<0.03	<0.02	<0.02	0.16	<0.03	<0.03	<0.03	<0.04	<0.03
Exp-B	0.03			0.001		0.02	0.16		0.001			
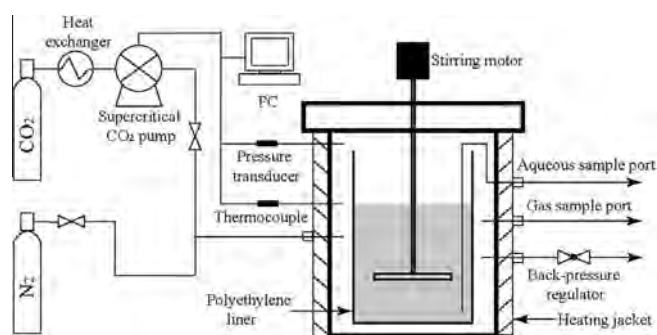
Fig. 2. Schematic diagram of reaction system. Modified after Lu et al. (2014).

unaffected, some small dissolution pits formed at the reacted grain surface, which indicates slight dissolution (Fig. 4f).

Mineral grains at the reaction interface were loosened because of loss of cement materials. Grain adjustment took place, with some grains sinking and some rising. A small amount of salt precipitated at the surface because of drying of the remaining reaction brine after the experiment (Fig. 5f). Calcite precipitation also occurred during the experiments, although calcite experienced net dissolution into the solution based on the results of SEM and aqueous chemistry. In Fig. 5a–c, for example, some calcite crystals grew out of the ion-milled plane and into the dissolution pores created from total dissolution of a dolomite rhomb. In Fig. 5i and l, calcite grains grew during the experiment, becoming higher than the original reaction surface and some overlying the surrounding quartz grains. The local growth of calcite suggests that dissolution of calcite is a dynamic process in which precipitation also occurs simultaneously at suitable locations. In other words, material transfer between solution and solid phases occurs as two-way traffic.

5.3. Reaction with sc-CO$_2$ (Exp-C)

During Exp-C, the ion-milled rock surface was also altered to some degree by the sc-CO$_2$ (Fig. 6). Major changes observed include etching of calcite grain surface and growth of salt crystals. Salt crystals precipitated mostly along grain boundaries

(Fig. 6c and d). The majority of newly formed salt is sodium chloride (halite). A small number of anhydrite needles were also observed at grain surface (Fig. 6g and h). EDS analysis was conducted on this reacted sample to show distribution of salt.

All calcite surfaces were corroded and rugged, but calcite grain surfaces were mostly on the same level of the ion-milled surface (Fig. 6l and p). Calcite may have been dissolved and reprecipitated elsewhere, with little mass loss to the fluid phase. Pyrite was slightly altered, with fibers and needles formed at its surface (Fig. 6o). Dolomite was not affected; its polished surface remained intact (Fig. 6c and d). All other minerals showed no evidence of reaction. The alteration of calcite and pyrite was likely facilitated by the presence of water retained in the pores. When pore water evaporated into sc-CO$_2$, it served as a carrier, constantly dissolving and precipitating a small amount of materials at the rock–gas interface. Only ~8 g of core chips were used in the 250 mL reactor. Assuming a residual water saturation of 25% and a rock porosity of 10% yielded a total of ~0.081 g of water present in the reactor (as opposed to ~110 g in the brine and CO$_2$ experiments). Despite the small amount of water available, the mineral surface was etched significantly.

5.4. Comparison of XRD mineral composition

In the unreacted sample, XRD results (Table 3) showed that quartz, dolomite, and calcite were the dominant mineral phases, followed by small amounts of K-feldspar, plagioclase (albite), muscovite, and pyrite. Common reactive mineral phases in the unreacted sample include dolomite (22.2%), calcite (7.0%), K-feldspar (4.2%), albite (2.1%), and pyrite (0.7%).

After subsampling for MICP tests, the remaining parts of the reacted samples of Exp-A and Exp-B were not sufficient in volume to be analyzed separately. The two reacted samples were combined for XRD analysis. The reacted sample of Exp-D was also analyzed by XRD. Mineral composition of the reacted samples was similar to that of the unreacted, with only small variations in mineral abundance. Because of the destructive nature of the XRD method, different rock chips from the same sample block were used for each analysis. Mineralogy variations across laminations and beds can lead to differences in XRD results. Variations measured in these samples are likely related to heterogeneity between the samples
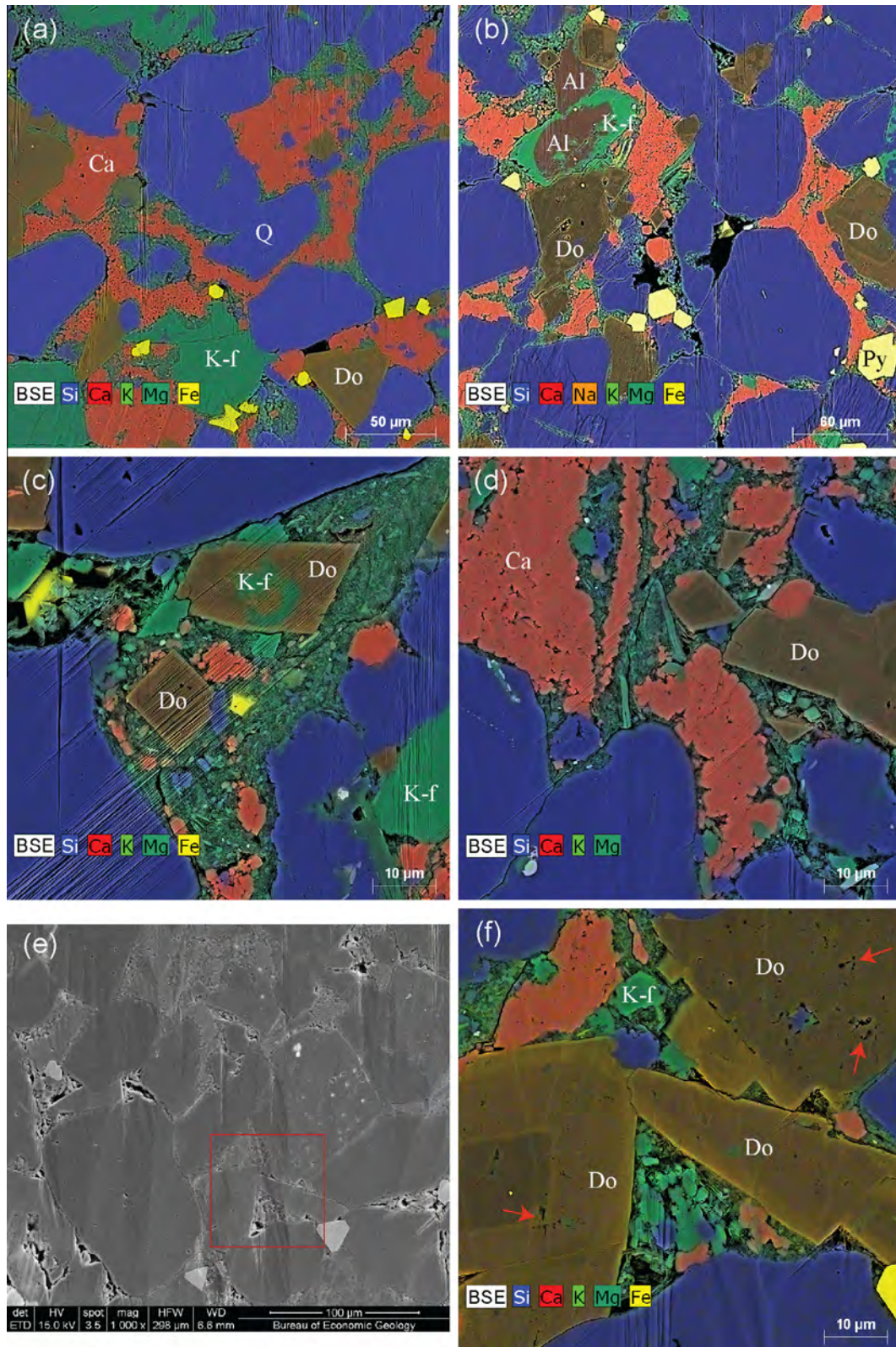
Fig. 3. SEM images and EDS maps of the unreacted Bakken sample. (a) Majority of framework grains are detrital quartz (Q) and K-feldspar (K-f). Abundant authigenic calcite (Ca), dolomite (Do), and pyrite (Py) largely eliminated primary pores. (b) Existing pores (dark) are mostly protected by detrital quartz grain. Ferroan dolomite tends to be euhedral and semi-euhedral, with visible growth bands. (c) Primary pores were eliminated by infills of authigenic calcite, dolomite, and pyrite and clay-sized particles. (d) Authigenic calcite and dolomite are the main pore-filling materials. (e) Secondary electron (SE) image shows occurrence of intergranular pores. Red box indicates area of Fig. 2f. (f) Submicron intraparticle pores (arrows) exist in authigenic dolomite and calcite.
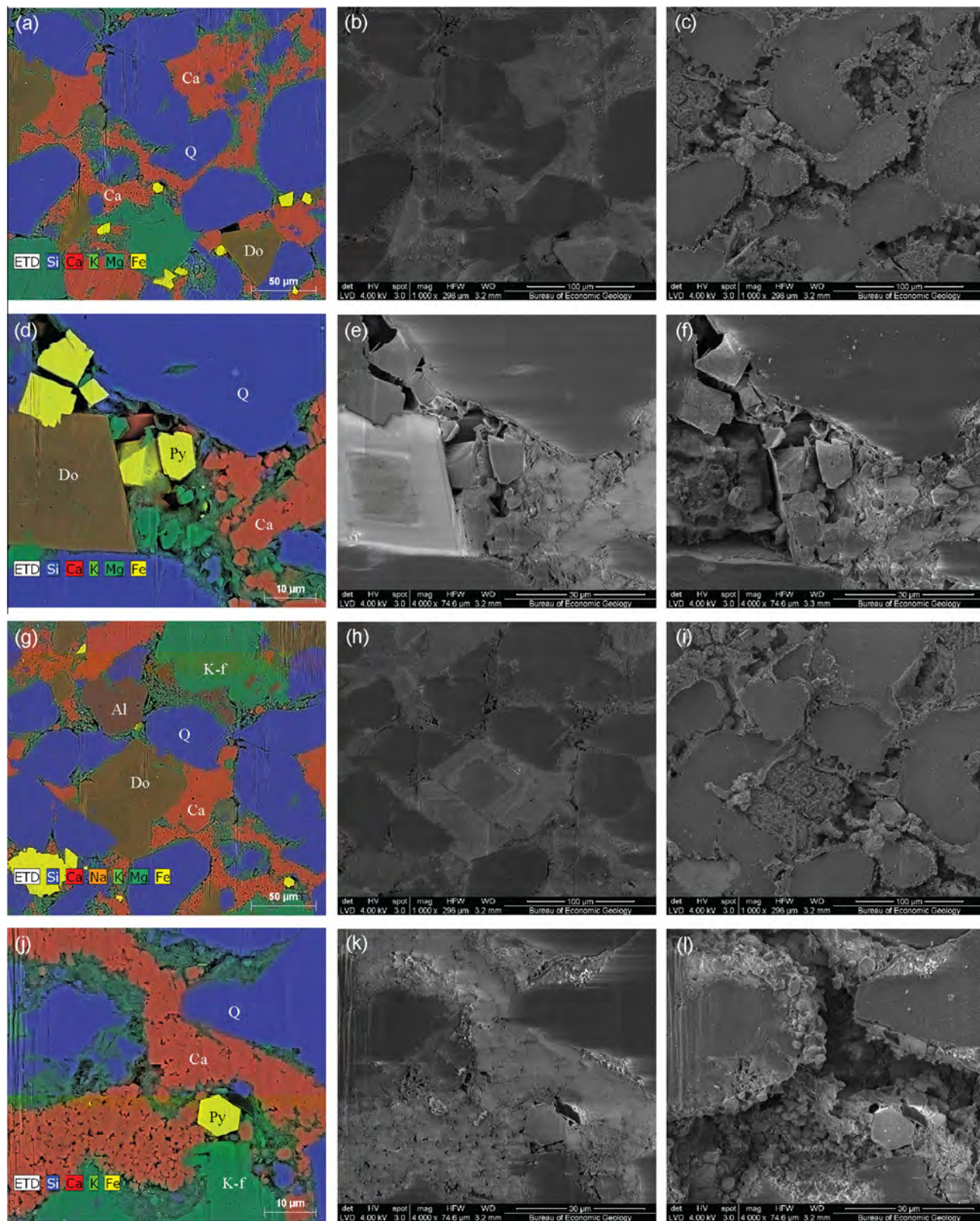
Fig. 4. Comparison of unreacted and reacted ion-milled sample of Exp-A. Left column (a, d, g, j): X-ray EDS element maps overlying BSE images of unreacted sample with iridium coating, showing false color for elements; middle column (b, e, h, k): low-vacuum detector (LVD) SE images of unreacted sample with coating removed; right column (c, f, i, l): LVD SE images of reacted sample without coating. Three images of each row cover the same area. Dissolution pits and holes were derived mostly from dissolution of calcite (Ca) and dolomite (Do).
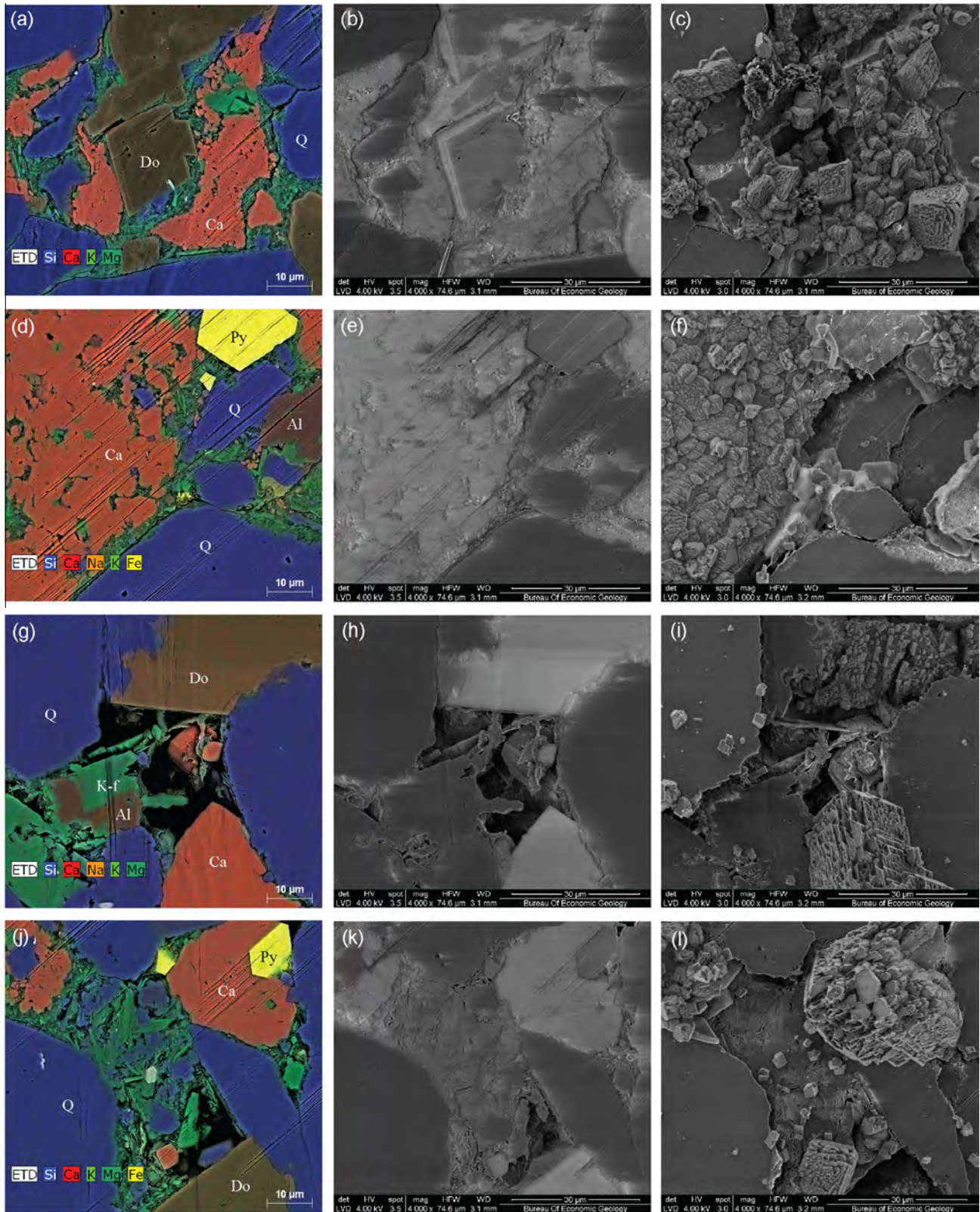
Fig. 5. Comparison of unreacted and reacted ion-milled sample of Exp-B. Left column (a, d, g, j): X-ray EDS element maps overlying BSE images of unreacted sample with iridium coating, showing false color for elements; middle column (b, e, h, k): low-vacuum detector (LVD) SE images of unreacted sample with coating removed; right column (c, f, i, l): LVD SE images of reacted sample without coating. Three images of each row cover the same area. Dissolution pits and holes were derived mostly from calcite (Ca) and dolomite (Do) dissolution. Calcite precipitation occurred locally.
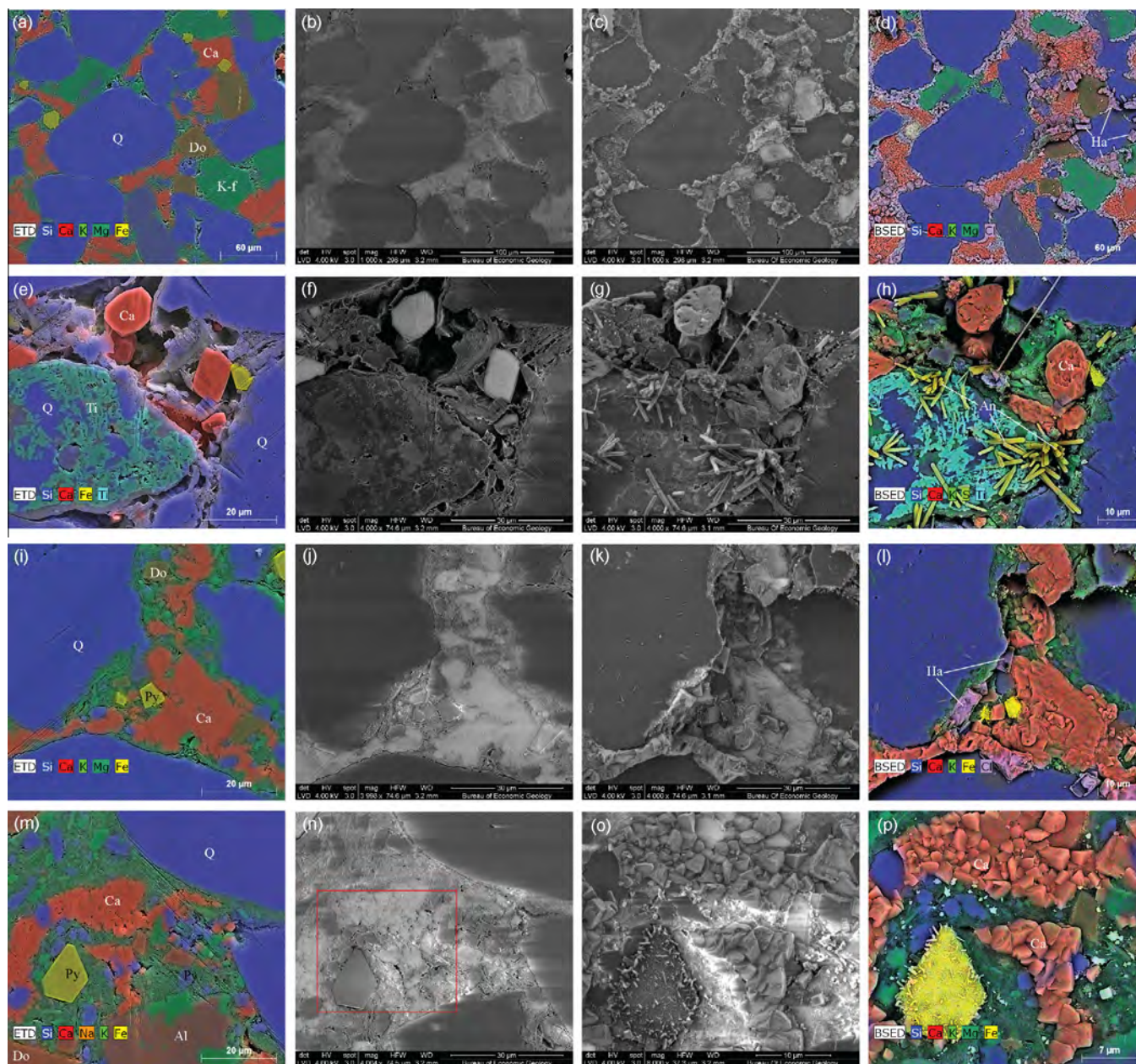
Fig. 6. Comparison of unreacted and reacted sample with dry, supercritical CO_2, Experiment Exp-C. First column (a, e, i, m): X-ray EDS element maps overlying BSE images of unreacted sample with iridium coating, showing false color for elements; second column (b, f, j, n): low-vacuum detector (LVD) SE images of the unreacted sample with coating removed; third column (c, g, k, o): LVD SE images of reacted sample without coating; fourth column (d, h, l, p): EDS maps overlying BSE SEM images of reacted sample with iridium coating. Images of each row cover the same area. Conductive coating was sputtered on reacted sample to aid identification of newly precipitated salts such as halite (purple) and anhydrite (yellow-green). Calcite surfaces are no long flat and show rugged morphology, but no net loss of calcite can be seen. (For interpretation of the references to color in this figure legend, the reader is referred to the web version of this article.)

Table 3
XRD mineral composition (%) of unreacted and reacted Bakken samples.

Experiment	Quartz	Illite	Calcite	Pyrite	Dolomite	K-feldspar	Albite	Muscovite
Unreacted	53.1	7.6	7.0	0.7	22.2	4.2	2.1	3.2
Exp-A & Exp-B	55.4	8.2	9.9	1.1	17.7	3.7	1.8	2.2
Exp-D	55.7	7.2	10.0	1.2	18.0	3.8	1.7	2.5

and the analytical error (up to 3%) of the XRD method (Hillier, 2000), not necessarily mineral–water reactions. For example, calcite abundance in reacted samples is ~3% higher than that of the unreacted sample, though SEM observation and aqueous chemistry clearly show calcite dissolution during the experiments. The XRD analytical error alone is higher than the amount of calcite dissolution measured in fluid chemistry in the experiments (~1%). For this reasons, the XRD method is not diagnostic of mineral reactions. Dolomite content is lower in reacted samples, which may partially reflect dolomite dissolution occurring during the experiments.

5.5. Geochemical evolution of reaction fluid

Although more realistic, the high salinity and complex composition of the synthetic brine used in the experiments caused two problems in the analytical results of the aqueous samples: (1) the high dilution factor (>900) led to a relatively large error in the IC and ICP results, and (2) high initial concentrations of several major and minor elements (Na, Ca, K, Cl, and other impurities) in the brine hampered the ability to discern temporal changes related to certain mineral reactions. Nevertheless, the high-frequency
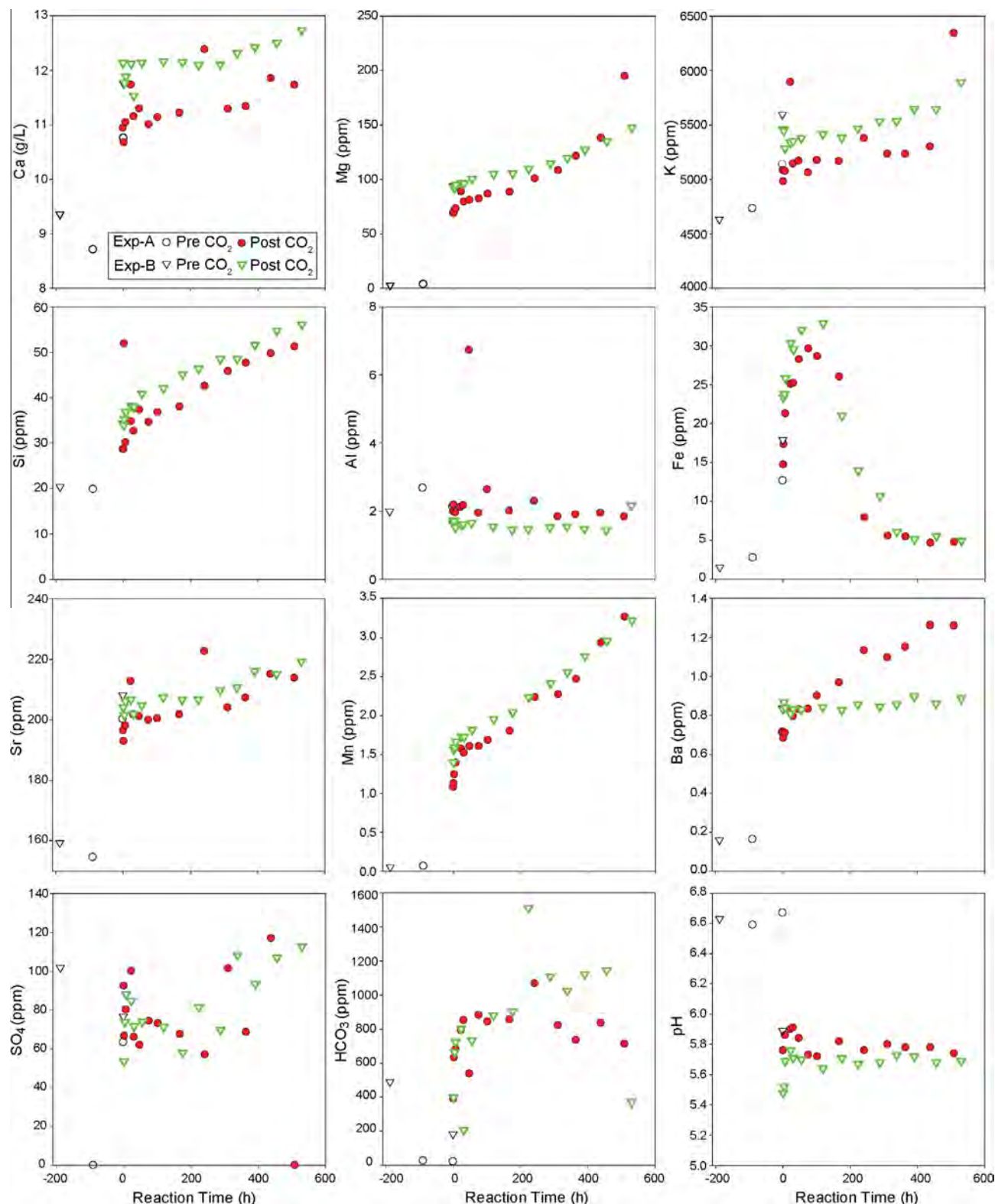

Fig. 7. Evolution of aqueous chemistry with time during Exp-A and Exp-B. Sulfate was analyzed by IC, HCO_3 measured by carbon analyzer, and pH measured on ~2 ml purged water at room temperature and atmospheric pressure. All others analyzed by ICP-MS.

aqueous chemical analyses do shed some light on the geochemical interactions of the Bakken reservoir rock and brine/CO_2.

Overall, the two brine experiments (Exp-A and Exp-B) showed very similar trends in the chemistry of the reaction fluid (except for Ba) (Table S1). Fig. 7 shows concentration changes with time in the two reaction experiments. The plots show three stages. The first fluid sample is equivalent to the first stage: the brine before it reacts with the rock. The second sample is taken just before Time 0, that is, just before CO_2 injection. In comparison to the first sample, the second sample reflects the impact of the brine on the rock; this lag time between the start of the exposure of the rock to the brine and CO_2 injection represents the second stage (3 and 8 days for Exp-A and Exp-B, respectively). The third stage is represented by all other data points that illustrate the impact of CO_2 on the rock–brine system.

The effect of brine is clearly visible, with a jump in concentrations of the major aqueous components between the first and second samples for all elements (Fig. 7). This period of time represents the process of establishing equilibrium between the synthetic brine and the rock sample. Carbonate dissolution is the most obvious effect of the brine, with Ca showing a net concentration increase to >10,000 ppm from <10,000 ppm, even accounting for the sampling drift (see Table S1). Mg, Mn, Sr, and Ba, generally associated with carbonates, show a similar effect to various degrees. This increase appears to be very quick and mostly occurs on the first day because the level of increase is similar for Exp-A (3 days' reaction) and Exp-B (8 days' reaction). The increase in aqueous concentrations is likely related to the synthetic brine being at a slightly lower total dissolved solids (TDS) than that of the actual Bakken brine, resulting in a disequilibrium in the rock–brine system.

The impact of CO_2 on the rock–brine system is manifest in the changes of chemical composition of the aqueous samples taken after CO_2 was added. The addition of CO_2 into the reactor led to a gradual increase for all elements except Al, which shows slow decreasing trends (Fig. 7). Ca shows the largest increase in concentration, followed by K, Mg, Si, Sr, Mn, and Ba (Fig. 7; Table S1). During the first day of CO_2 exposure, these cations showed the highest release rates, which gradually declined. Fe quickly rose to ∼30 ppm and then declined and stabilized at ∼5 ppm at the end of the experiments. Injection of CO_2 decreased pH from 6.6 to 5.5, followed by a quick rebound to stabilize at ∼5.8. DIC (HCO_3) quickly jumped from below 200 ppm to over 800 ppm during the first day after CO_2 was introduced.

Although precautions were taken to limit O_2 entry into the system, some may have remained in the reactor, as revealed by the increase in sulfate (early peak of ∼100 ppm, that is, 1 mmol) and Fe (early peak of 25–30 ppm, that is, 0.5 mmol; Fig. 7), matching the pyrite oxidation reaction that yields 0.5 mol Fe for each mol of sulfate. Given the amount of aqueous solution (110 mmol), this corresponds to 0.05 mmol of pyrite or <10% of the ∼1% pyrite present. After the early peak, Fe likely precipitates as FeOx, whereas sulfate concentrations start increasing again, albeit at a slower rate, after a dip of short duration. Sulfate shows a more complex behavior, with several concentration swings (Fig. 7) that are somewhat subject to cautious interpretation: the results are close to the detection limit, but both Exp-A and Exp-B show the same behavior, suggesting the results are real. If the first peak can be related to pyrite dissolution and initial O_2 consumption, the second slow concentration increase is more problematic.

Some silicate precipitation occurs as Al concentrations decrease and stay low despite the overall increase in Si concentrations (Fig. 7). No significant amount of exchangeable clay seems to be present in the rock sample. Ca/Na ion exchange, if it exists, would be difficult to observe because of the high concentration of these two elements in the brine. The relatively small amount of Ca, even

with the additional amount released by calcite dissolution that is generally favored by clays, is overwhelmed by the large Na concentration.

6. Discussion

During the process of CO_2-based fracturing, several geochemical regimes will form along the newly formed fractures. Early in the process, a single-phase regime will exist in the fractures, which are filled with sc-CO_2 and little water. Away from the fractures, in the rock matrix, sc-CO_2 will quickly saturate with water vapor and dissolve into the water. At later times, a dry sc-CO_2 regime will probably disappear as the CO_2 phase is gradually saturated with water, especially if there is a lengthy shut-in period. The volume of CO_2-rich formation water will gradually increase with time.

In the single-phase CO_2 regime (Exp-C and Exp-D), geochemical alteration of the reservoir rock is minimal because of the lack of liquid water. Though widespread surface corrosion was observed on calcite grains, net dissolution is negligible. Calcite is redistributed at the rock–CO_2 interface. As the small amount of water is wicked from the rock and partitions mostly in the sc-CO_2 phase, it acts as an agent for dissolution and subsequent precipitation of calcite but also leaves behind salt deposits that can be a concern for rock properties. Previous experimental studies of rock/mineral and water-saturated sc-CO_2 show mineral dissolution and precipitation on dolomite (Wang et al., 2013), forsterite (Kwak et al., 2011), and granite (Lin et al., 2008). Even at water contents below saturation, water vapor can form a thin film of liquid a few nanometers thick at mineral surfaces that facilitates mineral reactions by serving as a transport medium (Kwak et al., 2011). Under the experiment conditions of this study (115 °C and 300 bar), water is saturated in sc-CO_2 with a H_2O/CO_2 molar ratio of ∼0.025 (Spycher et al., 2003). In Exp-C and Exp-D, vapor was supplied by the residual pore water (<0.081 g) in the 250-mL reactor, which gives a H_2O/CO_2 molar ratio <1×10^{-6}. Previous experiments tested reactivity of sc-CO_2 with much higher water contents (Lin et al., 2008; Kwak et al., 2011; Wang et al., 2013). Our results suggest that even with such a low water content in sc-CO_2, carbonate dissolution and precipitation will occur.

The salts observed in Exp-C were formed from evaporation of residual pore water into dry sc-CO_2. Judging from the relatively large amount of precipitate at the reaction surface, migrating pore water would have carried the majority of the dissolved salts to the sample surface before evaporating, i.e., transferred the salts from inside the rock chip to its surface. During the process of CO_2-based fracturing, if the injected CO_2 is not water saturated, salt precipitation at fracture walls could bring adverse effects to production if significant amounts of dissolved salts are transferred to and accumulate at the rock–CO_2 interface as a result of evaporation of large volumes of pore water. Salt screens could form and inhibit hydrocarbon flow from matrix to the fractures, which may require additional treatment with fresh water.

In the CO_2-saturated water zone surrounding the pure CO_2, rock–water interactions will be triggered by lower pH resulting from CO_2 dissolution into the formation water. Potential reaction pathways in this region have been extensively investigated in permeable sandstones and carbonates by computer simulation (e.g., Gunter et al., 1997; Xu et al., 2003, 2005, 2010; Knauss et al., 2005; Zhang et al., 2015), laboratory experiments (Fischer et al., 2010; Chopping and Kaszuba, 2012; Yu et al., 2012; Lu et al., 2014; Huq et al., 2015), and field observation (Emberley et al., 2005; Kharaka et al., 2006; Mito et al., 2008; Lu et al., 2012). Mineral–water reactions that occurred in the two brine–CO_2 experiments (Exp-A and Exp-B) are similar to observations in previous studies.

In this study, changes of aqueous chemistry before addition of CO_2 reflects the process of water–rock equilibration. Upon CO_2 addition, elevated cation and anion concentrations indicate mineral reactions driven by CO_2. Dissolution of calcite and dolomite are the dominant mineral reactions. Besides being visible in SEM photos, release of cations such as Ca, Mg, Sr, and Mn into the synthetic brine indicates dissolution of the carbonate minerals. Mg is sourced from dolomite or Mg-bearing calcite. Minor cations such as Mn, Sr, and Ba show concentration trends similar to those of Ca and Mg. Dissolution of carbonate minerals is most likely the source of Mn, Sr, and Ba, as the minerals usually contain trace amounts of the metals. The fast increase in alkalinity observed right after CO_2 was introduced also indicates carbonate dissolution.

Interestingly, calcite reaction in the brine and CO_2 experiments proved to also be a dynamic process; localized calcite precipitation was observed at the reaction surface, although overall, calcite suffered net dissolution. Some portion of calcite was merely transported through the aqueous phase and redistributed in the rock samples. Local precipitation was likely caused by localized and temporal oversaturation of calcite. Although the reaction fluid was constantly stirred, some degree of chemical heterogeneity may still exist at the rock surface because of mineralogy heterogeneity and surface relief. During the operation, formation fluid is not as well mixed as in the experiment, and fluid chemistry will be more heterogeneous, leading to more-pronounced variations of mineral reactions; the overall effect of mineral reactions on pore network would be more complex and would need further investigation.

Minor feldspar dissolution also occurred in Exp-A and Exp-B, as shown by the increase of Si and K in the reaction solution (Fig. 7). Another mineral reaction is pyrite oxidation (observed in SEM), which resulted in an increase of sulfate concentration in the reaction solution. Although the reaction system was flushed by N_2 to remove air, a small amount of oxygen may have remained in the solution, headspace, or core chips, leading to oxidation of pyrite.

6.1. CO_2 impact on porosity and permeability

MICP porosity and calculated permeability results are listed in Table 4. Measured porosity of the reacted samples with brine and CO_2 (Exp-A and Exp-B) is over 3% higher than that of the unreacted samples (Fig. 8). Permeability is over 2 times higher. It should be noted that before permeability calculation, dissolution pits and holes formed at the sample surface are excluded as surface roughness and irregularity by conformance correction, which removes the pressure at which mercury starts intruding into the pores from capillary pressure curves. The surface dissolution holes were also excluded as surface irregularity for porosity calculation. Therefore, MICP porosity is much lower than the dissolution area at the reacted surface observed by SEM. The CO_2-reacted sample (Exp-D; repeat of Exp-C) shows much smaller changes in porosity and permeability, with slightly higher porosity and lower permeability than that of the unreacted sample.

Pore-size distribution of the samples is shown in Fig. 9. Pores <3.6 nm are not accessed by mercury intrusion because of limited intrusion pressure (60,000 psi). The majority of pore-throat sizes in the samples are between tens of nanometers and several microns.

Table 4
MICP porosity and permeability for unreacted and reacted samples.

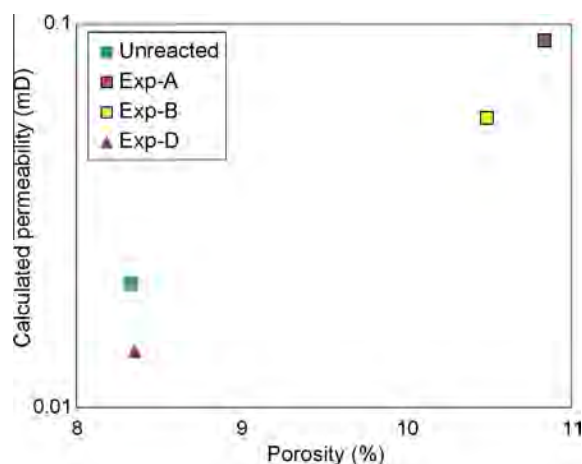| Sample	Porosity (%)	Permeability (md)	Density (g/cc)
Unreacted	8.33	0.02105	2.4721
Exp-A	10.84	0.09039	2.4685
Exp-B	10.49	0.05686	2.4616
Exp-D	8.35	0.01404	2.4933

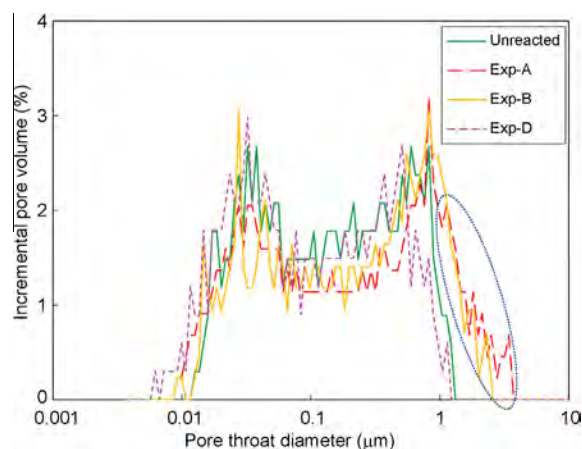**Fig. 8.** Porosity and permeability of unreacted and reacted samples measured in MICP tests.

Fig. 9. Pore-throat size distribution of unreacted (green) and reacted samples. Exp-A and Exp-B samples reacted with brine and CO_2 show higher proportion of large pore-throat size than that of the unreacted sample. Dashed circle highlights higher proportion of large pores. Exp-D sample reacted with pure CO_2 shows a small reduction of overall pore size. (For interpretation of the references to color in this figure legend, the reader is referred to the web version of this article.)

The pore-size distribution diagram shows a bimodal pattern, with a small pore-throat group of 30 nm and a large group of 0.5–0.9 μm.

Pore-throat size distribution curves of the reacted Exp-A and Exp-B samples show a similar pattern but with a higher proportion of large pores in the 1–3 μm range than that in the unreacted sample (Fig. 9), suggesting that mineral dissolution increased the overall pore size. The Exp-D sample shows very little change in pore-throat size distribution compared to that of the unreacted sample. Exp-D shows only a slight shift toward the left, which may indicate a small decrease of pore size (slightly lower permeability), suggesting that carbonate redistribution and salt precipitation observed at the reaction surface did not significantly alter the pore network.

The overall effect of CO_2–rock–water interactions on flow properties is positive, as shown in the MICP results (Fig. 7). Mineral dissolution created relatively large pores (Fig. 9). Increased porosity and permeability, as shown in the two reacted samples with brine and CO_2, would benefit hydrocarbon flow from rock matrix to fractures. However, rock mechanical strength may be compromised because of dissolution of cements, which may promote collapse of fracture walls and partial closure of fractures. The potential effect of cement dissolution requires further investigation.

7. Conclusions

This study evaluated the potential impact of mineral reactions on a pore system when CO_2 instead of water is used to complete wells with hydraulic fracturing. Autoclave experiments were conducted by exposing middle Bakken core fragments to CO_2-saturated synthetic brine and dry sc-CO_2. The mineral composition of the tested cores consisted mostly of nonreactive quartz, clays, and micas (illite and muscovite), as well as feldspars and abundant reactive carbonates. A minor amount of pyrite was also present. When brine was added, three main geochemical reactions were identified: dissolution of calcite and dolomite, precipitation of calcite, and some pyrite oxidation. Dissolution of calcite, the dominant reaction, created large dissolution pores and increased the porosity and permeability of the core samples. When only sc-CO_2 was used, calcite grain surfaces were altered by dissolution and precipitation while dolomite was not impacted. Salts such as halite and anhydrite were formed at rock surface by evaporating residual pore water into sc-CO_2. Overall, the presence of brine resulted in a net mass loss from the rock and a slight increase in porosity and doubling of permeability. sc-CO_2 with a trace amount of water vapor did not cause notable changes of rock properties except a slight decrease of permeability because of salt buildup at the rock–CO_2 interface. In the water zone, if the reprecipitation of some of the dissolved materials does not impede fluid flow to a great extent, the increase in rock permeability is advantageous for CO_2-based fracturing applications, notably when a large number of unpropped fractures are created. The uneven dissolution of rock materials generates rough surfaces, which act against the closure of the created fracture, a phenomenon that improves the residual conductivity of the fracture (Fredd et al., 2001) and that could improve production over time.

Acknowledgments

Appendix A. Supplementary data

Supplementary data associated with this article can be found, in the online version, at http://dx.doi.org/10.1016/j.juogr.2016.03.002.

References

Atrens, A.D., Gurgenci, H., Rudolph, V., 2008. CO_2 thermosiphon for competitive geothermal power generation. Energy Fuels 23, 553–557.

Bish, D.L., 1994. Quantitative x-ray diffraction analysis of soil. In: Amonette, J.E., Zelazny, L.W. (Eds.), Quantitative Methods in Soil Mineralogy. Soil Science Society of America, Wisconsin, pp. 267–295.

Brown, D.W., 2000. A hot dry rock geothermal energy concept utilizing supercritical CO_2 instead of water. In: Proceeding of the 25th Workshop on Geothermal Reservoir Engineering, Stanford, California, SGP-TR-165.

Brown, D.W., 2003. Geothermal energy production with supercritical fluids. US Patent, No. 6,668,554.

Cheng, Y., 2012. Impact of water dynamics in fractures on the performance of hydraulically fractured wells in gas-shale reservoirs. J. Can. Pet. Technol. 51 (2), 143–159. http://dx.doi.org/10.2118/127863-PA, SPE-127863-PA..

Chopping, C., Kaszuba, J.P., 2012. Supercritical carbon dioxide–brine–rock reactions in the Madison Limestone of Southwest Wyoming: an experimental investigation of a sulfur-rich natural carbon dioxide reservoir. Chem. Geol. 322–323 (5), 223–236. http://dx.doi.org/10.1016/j.chemgeo.2012.07.004.

Comisky, J.T., Newsham, K., Rushing, J.A., Blasingame, T.A., 2007. A comparative study of capillary-pressure-based empirical models for estimating absolute permeability in tight gas sands. In: Society of Petroleum Engineers Annual Technical Conference and Exhibition, Anaheim, California, 11-14 November. http://dx.doi.org/10.2118/110050-MS, SPE Paper 110050-MS.

Emberley, S., Hutcheon, I., Shevalier, M., Durocher, K., Mayer, B., Gunter, W.D., Perkins, E.H., 2005. Monitoring of fluid–rock interaction and CO_2 storage through produced fluid sampling at the Weyburn CO_2-injection enhanced oil recovery site, Saskatchewan Canada. Appl. Geochem. 20 (6), 1131–1157. http://dx.doi.org/10.1016/j.apgeochem.2005.02.007.

Fischer, S., Liebscher, A., Wandrey, M., 2010. CO2–brine–rockinteraction—first results of long-term exposure experiments at in situ P-T conditions of the Ketzin CO_2 reservoir. Chem. Erde- Geochem. 70 (30), 155–164. http://dx.doi.org/10.1016/10.1016/j.chemer.2010.06.001.

Fredd, C.N., McConnell, S.B., Boney, C.L., England, K.W., 2001. Experimental study of fracture conductivity for water-fracturing and conventional fracturing applications. SPE J. 6 (3), 288–298. http://dx.doi.org/10.2118/74138-PA, SPE 74138-PA..

Garbis, S.J., Taylor, J.L., 1986. The utility of CO_2 as an energizing component for fracturing fluids. SPE Prod. Eng. 1 (5), 351–358. http://dx.doi.org/10.2118/13794-PA, SPE-13794-PA.

Gunter, W.D., Wiwehar, B., Perkins, E.H., 1997. Aquifer disposal of CO_2-rich greenhouse gases: extension of the time scale of experiment for CO_2-sequestering reactions by geochemical modelling. Mineral. Petrol. 59 (1–2), 121–140. http://dx.doi.org/10.1007/BF01163065.

Harris, P.C., Haynes, R.J., Egger, J.P., 1984. The use of CO_2-based fracturing fluids in the Red Fork Formation in the Anadarko Basin, Oklahoma. J. Pet. Technol. 36 (6), 1003–1008. http://dx.doi.org/10.2118/11575-PA, SPE-11575-PA..

Hillier, S., 1999. Use of an air brush to spray dry samples for X-ray powder diffraction. Clay Miner. 34 (1), 127–135. http://dx.doi.org/10.1180/000985599545984.

Hillier, S., 2000. Accurate quantitative analysis of clay and other minerals in sandstones by XRD: comparison of a Rietveld and a reference intensity ratio (RIR) method and the importance of sample preparation. Clay Miner. 35, 291–302.

Huq, F., Haderlein, S.B., Cirpka, O.A., Blum, P., Grathwohl, P., 2015. Flow-through experiments on water–rock interactions in a sandstone caused by CO_2 injection at pressures and temperatures mimicking reservoir conditions. Appl. Geochem. 58, 136–146. http://dx.doi.org/10.1016/j.apgeochem.2015.04.006.

Jacobs, T., 2014. Energized fractures: shale revolution revisits the energized fracture. J. Pet. Technol. 66 (6), 48–56. http://dx.doi.org/10.2118/0614-0048-JPT.

Johnson, J.W., Nitao, J.J., Morris, J.P., 2005. Modeling the long-term isolation performance of natural and engineered geologic CO_2 storage sites. Greenhouse Gas Control Technol. 2 (1), 1315–1321. http://dx.doi.org/10.1016/B978-008044704-9/50144-0.

Jun, Y.S., Giammar, D.E., Werth, C.J., 2013. Impacts of geochemical reactions on geologic carbon sequestration. Environ. Sci. Technol. 47 (1), 3–8. http://dx.doi.org/10.1021/es3027133.

Kharaka, Y.K., Cole, D.R., 2011. Geochemistry of geologic sequestration of carbon dioxide. In: Harmon, R. (Ed.), Frontiers in Geochemistry: Contribution of Geochemistry to the Study of the Earth. Wiley-Blackwell, pp. 135–169, Chapter 8.

Kharaka, Y.K., Cole, D.R., Hovorka, S.D., Gunter, W.D., Knauss, K.G., Freifeld, B.M., 2006. Gas–water–rock interactions in Frio Formation following CO_2 injection: implications for the storage of greenhouse gases in sedimentary basins. Geology 34 (7), 577–580. http://dx.doi.org/10.1130/G22357.1.

Knauss, K.G., Johnson, J.W., Steefel, C.I., 2005. Evaluation of the impact of CO_2, co-contaminant gas, aqueous fluid, and reservoir rock interactions on the geologic sequestration of CO_2. Chem. Geol. 217 (3–4), 339–350. http://dx.doi.org/10.1016/j.chemgeo.2004.12.017.

Kwak, J.H., Hu, J.Z., Turcu, R.V.F., Rosso, K.M., Ilton, E.S., Wang, C., Sears, J.A., Engelhard, M.H., Felmy, A.R., Hoyt, D.W., 2011. The role of H_2O in the carbonation of forsterite in supercritical CO_2. Int. J. Greenhouse Gas Control 5 (4), 1081–1092. http://dx.doi.org/10.1016/j.ijggc.2011.05.013.

Liao, S., Brunner, F., Mattar, L., 2009. Impact of ignoring CO_2 injection volumes on post-frac PTA. In: Canadian International Petroleum Conference, Calgary, Alberta, Canada, 16–18 June. http://dx.doi.org/10.2118/2009-124, PETSOC-2009-124.

Lin, H., Fujii, T., Takisawa, R., Takahashi, T., Hashida, T., 2008. Experimental evaluation of interactions in supercritical CO_2/water/rock minerals system under geologic CO_2 sequestration conditions. J. Mater. Sci. 43, 2307–2315. http://dx.doi.org/10.1007/s10853-007-2029-4.

Lu, J., Partin, J.W., Hovorka, S.D., Wong, C., 2010. Potential risks to freshwater resources as a result of leakage from CO_2 geological storage: a batch-reaction experiment. Environ. Earth Sci. 60 (2), 335–348. http://dx.doi.org/10.1007/s12665-009-0382-0.

Lu, J., Milliken, K., Reed, M.R., Hovorka, S., 2011. Diagenesis and sealing capacity of the middle Tuscaloosa mudstone at the Cranfield carbon dioxide injection site.

Mississippi Environ. Geosci. 18 (1), 35–53. http://dx.doi.org/10.1306/eg.09091010015.

Lu, J., Kharaka, Y.K., Thordsen, J.J., Horita, J., Karamalidis, A., Griffith, C., Hakala, J.A., Ambats, G., Cole, D.R., Phelps, T.J., Manning, M.A., Cook, P.J., Hovorka, S.D., 2012. CO_2-rock-brine interactions in lower Tuscaloosa Formation at Cranfield CO_2 sequestration site, Mississippi, U.S.A. Chem. Geol. 291, 269–277. http://dx.doi.org/10.1016/j.chemgeo.2011.10.020.

Lu, J., Mickler, P.J., Nicot, J.-P., Yang, C., Romanak, K.D., 2014. Geochemical impact of oxygen on siliciclastic carbon storage reservoirs. Int. J. Greenhouse Gas Control 21, 214–231. http://dx.doi.org/10.1016/j.ijggc.2013.12.017.

Middleton, R., Viswanathan, H., Currier, R., Gupta, R., 2014. CO_2 as a fracturing fluid: potential for commercial-scale shale gas production and CO_2 sequestration. in: Proceeding of 12th International Conference on Greenhouse Gas Control Technologies, Austin, Texas 5–9 October, Energy Procedia 63, pp. 7780–7784. doi: http://dx.doi.org/10.1016/j.egypro.2014.11.812.

Mito, S., Xue, Z., Ohsumi, T., 2008. Case study of geochemical reactions at the Nagaoka CO_2 injection site. Japan. Int. J. Greenhouse Gas Control 2 (3), 309–318. http://dx.doi.org/10.1016/j.ijggc.2008.04.007.

Pruess, K., 2006. Enhanced geothermal systems (EGS) using CO_2 as working fluid—a novel approach for generating renewable energy with simultaneous sequestration of carbon. Geothermal 35 (4), 351–367. http://dx.doi.org/10.1016/j.geothermics.2006.08.002.

Ribeiro, L.H., Sharma, M.M., 2012. Multiphase fluid-loss properties and return permeability of energized fracturing fluids. SPE Prod. Oper. 27 (3), 265–277. http://dx.doi.org/10.2118/139622-PA, SPE 139622-PA..

Ribeiro, L.H., Li, H., Bryant, J.E., 2015. Use of CO2-hybrid fracturing design to enhance production from unpropped fractured networks. in: SPE Hydraulic Fracturing Technology Conference, The Woodlands, Texas, 3–5 February. SPE-173380-MS. http://dx.doi.org/10.2118/173380-MS.

Scanlon, B.R., Reedy, R.C., Nicot, J.-P., 2014. Comparison of water use for hydraulic fracturing for shale oil and gas production. Environ. Sci. Technol. 48 (20), 12386–12393. http://dx.doi.org/10.1021/es502506v.

Shafer, J., Neasham, J., 2000. Mercury porosimetry protocol for rapid determination of petrophysical and reservoir quality properties. Proceeding of the International Symposium of the Society of Core Analysts, SCA, 2000–2021.

Sinal, M.L., Lancaster, G., 1987. Liquid CO_2 fracturing: advantages and limitations. J. Can. Pet. Technol. 26, 26–30. http://dx.doi.org/10.2118/87-05-01, PETSOC-87-05-01..

Spycher, N., Pruess, K., Ennis-King, J., 2003. CO_2-H_2O mixtures in the geological sequestration of CO_2. I. Assessment and calculation of mutual solubilities from 12 to 100 °C and up to 600 bar. Geochim. Cosmochim. Acta 67 (16), 3015–3031. http://dx.doi.org/10.1016/S0016-7037(03)00273-4.

Sun, H., Yao, J., Gao, S., Fan, D., Wang, C., Sun, Z., 2013. Numerical study of CO_2 enhanced natural gas recovery and sequestration in shale gas reservoirs. Int. J. Greenhouse Gas Control 19, 406–419. http://dx.doi.org/10.1016/j.ijggc.2013.09.011.

Wang, X., Alvarado, V., Swoboda-Colberg, N., Kaszuba, J.P., 2013. Reactivity of dolomite in water-saturated supercritical carbon dioxide: significance for carbon capture and storage and for enhanced oil and gas recovery. Energy Convers. Manage. 65, 564–573. http://dx.doi.org/10.1016/j.enconman.2012.07.024.

White, S.P., Allis, R.G., Moore, J., Chidsey, T., Morgan, C., Gwynn, W., Adams, M., 2005. Simulation of reactive transport of injected CO_2 on the Colorado Plateau. Chem. Geol. 217 (3–4), 387–405. http://dx.doi.org/10.1016/j.chemgeo.2004.12.020.

Xu, T., Apps, J.A., Pruess, K., 2003. Reactive geochemical transport simulation to study mineral trapping for CO_2 disposal in deep arenaceous formations. J. Geophys. Res. 108 (B2), 3–13. http://dx.doi.org/10.1029/2002JB001979.

Xu, T., Apps, J.A., Pruess, K., 2005. Mineral sequestration of carbon dioxide in a sandstone–shale system. Chem. Geol. 217 (3–4), 295–318. http://dx.doi.org/10.1016/j.chemgeo.2004.12.015.

Xu, T., Kharaka, Y.K., Doughty, C., Freifeld, B.M., Daley, T.M., 2010. Reactive transport modeling to study changes in water chemistry induced by CO_2 injection at the Frio-I Brine Pilot. Chem. Geol. 271 (3–4), 153–164. http://dx.doi.org/10.1016/j.chemgeo.2010.01.006.

Yu, Z., Liu, L., Yang, S., Li, S., Yang, Y., 2012. An experimental study of CO_2–brine–rock interaction at in situ pressure–temperature reservoir conditions. Chem. Geol. 326–327, 88–101. http://dx.doi.org/10.1016/j.chemgeo.2012.07.030.

Zhang, L., Soong, Y., Dilmore, R., Lopano, C., 2015. Numerical simulation of porosity and permeability evolution of Mount Simon sandstone under geological carbon sequestration conditions. Chem. Geol. 403, 1–12. http://dx.doi.org/10.1016/j.chemgeo.2015.03.014.